Title: Local, transient tensile stress on the nuclear membrane causes membrane rupture

Authors: Qiao Zhang[†], Andrew C. Tamashunas[†], Ashutosh Agrawal[‡], Mehdi Torbati[‡], Aditya Katiyar[§], Richard B. Dickinson[†], Jan Lammerding[||], and Tanmay P. Lele[†,*]

Affiliations: [†] *Department of Chemical Engineering, University of Florida, Gainesville, FL 32611;* [‡] *Department of Mechanical Engineering, University of Houston, Houston, TX 7720;* [§]*Department of Mechanical and Aerospace Engineering, University of Florida, Gainesville, FL 32611; and* [||]*Weill Institute for Cell and Molecular Biology & Meinig School of Biomedical Engineering, Cornell University, Ithaca, NY 14853*

[*]Address correspondence to: Tanmay P. Lele (tlele@che.ufl.edu)
Department of Chemical Engineering, Bldg. 723
University of Florida, Gainesville, FL 32611
Ph: 352-392-0317

Running Head: Nuclear rupture under tensile stress

ABSTRACT

Cancer cell migration through narrow constrictions generates compressive stresses on the nucleus that deform it and cause rupture of nuclear membranes. Nuclear membrane rupture allows uncontrolled exchange between nuclear and cytoplasmic contents. Local tensile stresses can also cause nuclear deformations, but whether such deformations are accompanied by nuclear membrane rupture is unknown. Here we used a direct force probe to locally deform the nucleus by applying a transient tensile stress to the nuclear membrane. We found that a transient (~0.2 s) deformation (~1% projected area strain) in normal mammary epithelial cells (MCF-10A cells) was sufficient to cause rupture of the nuclear membrane. Nuclear membrane rupture scaled with the magnitude of nuclear deformation and the magnitude of applied tensile stress. Comparison of diffusive fluxes of nuclear probes between wild type and lamin-depleted MCF-10A cells revealed that lamin A/C, but not lamin B2, protects the nuclear membranes against rupture from tensile stress. Our results suggest that transient nuclear deformations typically caused by local tensile stresses are sufficient to cause nuclear membrane rupture.

INTRODUCTION

Cell migration through narrow constrictions causes nuclear deformations (Wolf *et al.*, 2013; Irianto *et al.*, 2017). These deformations can be accompanied by local rupture of the nuclear membrane (Denais *et al.*, 2016; Raab *et al.*, 2016). Exposing nuclear contents to the cytoplasm causes DNA damage (Denais *et al.*, 2016; Irianto *et al.*, 2017) that may contribute to cancer progression. In these situations, increased intranuclear pressure resulting from compressive cytoskeletal forces is thought to cause the formation of micron-sized membrane blebs that separate from the lamina and eventually rupture (Denais *et al.*, 2016; Hatch and Hetzer, 2016; Lammerding and Wolf, 2016). Such spontaneous membrane rupture occurs not only during cell migration in confined spaces but also in cultured cancer cells, likely due to actin confinement (Hatch and Hetzer, 2016).

Local tensile stresses can also cause nuclear deformations (Maniotis *et al.*, 1997; Lammerding *et al.*, 2006; Wang *et al.*, 2009; Chancellor *et al.*, 2010; Wu *et al.*, 2014; Alam *et al.*, 2015; Tajik *et al.*, 2016; Lele *et al.*, 2018). For example, extracellular stresses applied to integrin receptors on the cell membrane can be propagated to the nucleus through the cytoskeleton causing local nuclear deformations, rotations and translations (Maniotis *et al.*, 1997; Wang *et al.*, 2009; Tajik *et al.*, 2016). Tensile stresses on the nuclear surface are also generated during cell migration which can cause nuclear translations (Wu *et al.*, 2014). Also, local cell membrane protrusions proximal to the nuclear surface have been shown to cause local nuclear deformations (Alam *et al.*, 2015). Such tensile stresses are transmitted to the nuclear surface through molecular connections between nesprin proteins embedded in the outer nuclear envelope which bind to the cellular cytoskeleton(Luxton and Starr, 2014; Uhler and Shivashankar, 2017; Kirby and Lammerding, 2018; Lee and Burke, 2018). Because nesprins are embedded in the cell membrane and bind to SUN proteins that are also in the inner nuclear membrane, it is possible that tensile stresses exerted on these proteins may cause rupture of the nuclear membranes. However, whether such deformations are accompanied by nuclear membrane rupture has not been examined yet.

Here, we applied local tensile stress on the nuclear membranes in living adherent cells using a direct force probe (Neelam *et al.*, 2015; Zhang *et al.*, 2018) and examined nuclear membrane integrity

with previously established nuclear membrane rupture reporters (Denais *et al.*, 2016). Our results demonstrate that suggest that transient nuclear deformations typically caused by local tensile stresses are indeed sufficient to cause nuclear membrane rupture.

RESULTS

Using the direct force probe, we applied stress directly to the nuclear surface in an adherent living cell. The method involves suction-sealing a narrow micropipette to the nuclear surface.The suction pressure in the micropipette is known precisely (Neelam *et al.*, 2015; Zhang *et al.*, 2018). Moving the micropipette away from the nucleus deforms the nucleus locally. Eventually, the micropipette detaches when the restoring forces in the nucleus equal the applied suction pressure across the small nuclear membrane section. Using this method, we applied a short (< 1 s, see movie 1) force pulse of 2 nN over a circular area (diameter 0.5 μm) of the nucleus of a normal mammary MCF-10A epithelial cell expressing an EGFP-NLS nuclear rupture reporter. This force corresponds to a (nearly normal) stress of 10 kPa. The nucleus transiently deformed at the force application site; the deformation resulted in loss of nuclear membrane integrity (nuclear membrane rupture), as evidenced by the leakage of EGFP-NLS into the cytoplasm, resulting in a transient loss of nuclear EGFP-NLS fluorescence and a corresponding increase in the cytoplasmic EGFP-NLS signal (Figure 1A and corresponding intensities in plot 1B). By ~ 60 min after the end of the force pulse, the nuclear and cytoplasmic EGFP-NLS intensities recovered back to pre-force levels, indicating membrane repair and reimport of the EGFP-NLS reporter (Figure 1A, B). These results confirm that the initial decrease in EGFP-NLS corresponded to an actual rupture event. For additional confirmation, we modified cells to express cGAS-mCherry, a cytoplasmic DNA-binding protein that accumulates at the site of nuclear envelope rupture where the genomic DNA is exposed to the cytoplasm (Denais *et al.*, 2016). The rapid accumulation of cGAS-mCherry at the force application site indicated that the nuclear membrane rupture was local (Figure 1C, inserts for enlarged view).

We tested if the direct force probe causes consistent and reproducible rupture by analyzing the time-dependent decay in the nuclear EGFP-NLS intensity after the force pulse over several cells. Data

pooled from several probed cells showed a consistent decrease in the nuclear intensity upon application of the stress pulse, an increase in cytoplasmic intensity, and relatively small change in control cells (Figure 2A, control cells are unstressed, and in the same image as the stressed cell, which helps control for photobleaching effects). We quantified the extent of nuclear deformation by overlaying images of the nucleus before and at maximum deformation using the method in (Neelam *et al.*, 2015) (see materials and methods). A stress pulse of 10 kPa corresponded to an average area strain of 0.8% ± 0.1%. These data suggest that local tensile stresses resulting in transient nuclear deformations of the degree typically caused by local tensile stresses (Maniotis *et al.*, 1997; Lammerding *et al.*, 2005; Lammerding and Lee, 2009; Alam *et al.*, 2015; Tajik *et al.*, 2016) consistently rupture the nuclear membranes of MCF-10A cells.

To test the hypothesis that the extent of rupture depends on the magnitude of tensile stress applied by the direct force probe, we repeated these experiments over a range of applied nuclear membrane stresses. Figure 2B shows pooled data for dynamic decrease in nuclear EGFP-NLS intensity at different stress levels. There was a measurable decrease in the nuclear EGFP-NLS intensity in the nucleus at stresses as low as 2 kPa. The maximum loss of nuclear EGFP-NLS intensity (measured as the intensity at 120 s after the stress pulse, i.e. long enough for the nuclear EGFP-NLS intensity to fully decay) scaled with the magnitude of the nuclear membrane stress applied (Figure 2C). Histograms of EGFP-NLS intensity at 120 s also show a clear trend toward higher means at larger stress values with only a minor effect on the probability of rupture (Figure S1A). We confirmed a similar dependence of nuclear membrane rupture on applied membrane stress in mouse embryonic fibroblasts (MEFs) (Figure S2), indicating that the findings are not specific to a single cell line or species.

The underlying nuclear lamina may protect the nuclear membranes from rupture under tensile stress (Denais *et al.*, 2016; Hatch and Hetzer, 2016). We therefore depleted nuclear lamins and examined the effect on nuclear membrane rupture. Depletion of lamin A/C by siRNA (Figure S3), resulted in a higher loss of nuclear EGFP-NLS (Figure 3A), while depletion of lamin B2 had no significant effect (Figure 3B). This was surprising as previous studies with nuclear compression found that lamin B2 has a

protective role in nuclear membrane rupture (Hatch *et al.*, 2013; Bakhoum *et al.*, 2018). Given that loss of of lamin A/C softens the nucleus (Broers *et al.*, 2004; Lammerding *et al.*, 2004; Pajerowski *et al.*, 2007; Schäpe *et al.*, 2009; Swift *et al.*, 2013; Davidson *et al.*, 2015; Stephens *et al.*, 2017), we examined the effect of lamin depletion on nuclear deformation under transiently applied local nuclear membrane stress. Lamin B2 depletion had no effect on nuclear deformation (Figure S4), consistent with previous studies (Lammerding *et al.*, 2006), and correspondingly no effect on rupture (Figure 3D), while lamin A/C depletion resulted in larger nuclear deformation (and a larger extent of membrane rupture) (Figure 3C). The loss in nuclear EGFP-NLS intensity after rupture scaled with the stress levels and with the extent of maximum nuclear deformation under stress for both MCF-10A cells and for MEFs (Figure 3E).

To estimate the size of the membrane defect during nuclear rupture, we used the quantitative kinetic data on decrease of EGFP-NLS in the nucleus combined with finite element modeling (FEM) of the diffusion of EGFP-NLS through a small circular hole in the surface of the three dimensional nucleus separating the nucleus and the cytoplasm (Figure 4A shows a two dimensional projection of the three dimensional nucleus and cell). Notably, the calculations estimate an 'effective size', as it is possible that more than one smaller hole is created in the membranes, below the resolution limit of the light microscope. In this calculation, three dimensional cell and nuclear geometric parameters were chosen based on our previously published measurements with MCF-10A cells ((Neelam *et al.*, 2016), Table 1), and the diffusion coefficient of EGFP-NLS has been previously reported both in the cytoplasm and the nucleus ((Wu *et al.*, 2009), Table 1). EGFP-NLS is reimported from the cytoplasm into the nucleus, and this reimport rate depends on the cytoplasmic concentration and the number of nuclear pores and the efficiency of the nuclear transport mechanism (the latter are not easily measurable for a given cell). To avoid the complications of nuclear re-import, we modeled only the initial rates of loss of EGFP-NLS when the cytoplasmic intensity and hence the re-import rate are negligible. The FEM calculations yield the initial rate of NSF loss as a function of hole diameter (Figure 4B). Comparison between experimental and simulation data (Figure 4B and 4C) allowed us to estimate the force-dependent effective hole size

(Table 2). Our model indicates that these hole diameters are ~100 nm (ranging from ~ 96 nm at lower stresses to ~ 465 nm at higher stresses) in agreement with similar pore sizes used by others (Deviri *et al.*, 2017) and a previous estimate based on superresolution imaging (Denais *et al.*, 2016).

DISCUSSION

Both compressive and tensile stress can cause nuclear deformation. Compressive stresses can cause rupture of the nuclear membrane, thereby exposing nuclear contents to the cytoplasm. Whether tensile stress-induced deformations similarly cause nuclear membrane rupture is currently unknown. Here we used the direct force probe to apply tensile stresses directly to the nuclear surface. Our results provide the first evidence that a tensile stress applied locally and transiently on the nuclear surface that elicits elastic nuclear deformation is sufficient to cause transient nuclear membrane rupture. The extent of nuclear deformation required for rupture under tensile stresses is relatively modest (<1% projected area strain), and is typical of what has been reported for nuclear deformations under tensile stress (Maniotis *et al.*, 1997; Lammerding *et al.*, 2005; Lammerding and Lee, 2009; Alam *et al.*, 2015; Tajik *et al.*, 2016).

Because the nuclear membrane is not a single membrane, but consists of an outer and inner membrane fused to each other at several thousand nuclear pores, its mechanical rupture under a stress is expected to be different from the well-studied situation of rupture of a single free-standing membrane. In addition, proteins that localize in the membrane mechanically couple the two membranes; these include Sun1/2 proteins embedded in the inner nuclear- membrane that bind to nesprins embedded in the outer nuclear membrane (5-7). Also, proteins in the inner nuclear membrane (like emerin and farnesylated lamins) tether the inner nuclear membrane to the underlying nuclear lamina and chromatin providing structural support (Foisner, 2001; Dahl *et al.*, 2008; Isermann and Lammerding, 2013; Chang *et al.*, 2015). The direct force probe allowed us to quantitatively compare rupture behavior between wild type and lamin depleted cells, and also across cell types. Such comparisons are possible because the applied tensile stress is the same across these different conditions. We note here, that although the applied stress

is tensile (pulling), the mechanical response of nuclear components may be more complex, including possibly simultaneous compression of some elements, and bending and expansion of others.

Depletion of lamin A/C but not lamin B2 increased the loss in EGFP-NLS nuclear intensity under stress. The probability of rupture was not significantly altered upon depletion of lamin A/C (Figure S1B), suggesting that the larger loss of intensity corresponded to a larger effective hole size. The hole size estimated by comparison with the finite element calculations was ~ 433 nm for lamin A/C depletion (228 nm for the scrambled control) and 198 nm for lamin B2 depletion (223 nm for the scrambled control). This suggests that lamin A/C but not lamin B2 plays a protective role in preventing rupture under tensile stresses.

The fact that the deformation scales with the applied stress (as we have previously reported (Neelam *et al.*, 2015)) indicates that the rupture process itself does not cause detachment from the micropipette. If the small patch of nuclear membranes in contact with the pipette tip was being torn away from the nucleus due to pipette motion, then the pipette would detach when this rupture occurred, and nuclear deformation would be independent of the suction pressure. Further, applying suction alone to the nuclear membrane without pulling on it did not change EGFP-NLS intensity in the nucleus (Figure S6), arguing against the possibility that the applied suction pressure damages nuclear pores.

Here we have reported nuclear deformation in terms of the projected area strain. The local strains near the pipette tip are likely higher than the projected area strain. It is desirable to measure the actual membrane area strain caused by application of the tensile stresses (the critical lipid membrane strain for rupture is of the order of 2 % (Staykova *et al.*, 2011)), but it is difficult to accurately quantify this strain in our live cell imaging experiments because the nuclear shape itself is changing locally (which involves translation of the membranes in addition to membrane strain).

In single lipid bilayers, hole formation is determined by the energetic interplay between the surface tension in the bilayer and the line tension energy, which develops as a result of extreme bending of lipids at the pore interface (Gonzalez-Rodriguez *et al.*, 2012; Akimov *et al.*, 2017b, a). For such a

system, there is a critical radius on the order of few nanometers (Akimov *et al.*, 2017b, a). If the holes in single bilayers exceed this critical radius, they are unstable and expand continually. If the holes are smaller than the critical radius, they spontaneously close. However, our experiments suggest that the holes are much larger (order of 100 nm) and they are stable over several seconds. The mechanism underlying this stability are not clear.

The fact that the leakage through nuclear holes would require rupture of both the nuclear membranes leads us to speculate that stable holes may be due to the creation of a donut-shaped hole between the ONM and the INM. After the initial rapid formation of the hole (< 1 s), the hole may reach an equilibrium size over the several seconds after hole formation. We explored this speculative picture by modeling the geometry of such donut holes by minimizing the bending energy. This approach is similar to the one we adopted previously to explain the separation of bilayers in the nuclear envelope (Torbati *et al.*, 2016). It relies on the fact that a lipid bilayer is a 2D elastic sheet which is fluid in-plane allowing lipids to diffuse freely but resists out-of-plane bending deformations. We computed the equilibrium shapes of a donut hole for a prescribed membrane tension and appropriate boundary conditions (described in the Methods section). The calculation in Figure S5A (top) shows a prediction of ~ 60 nm three-dimensional donut-shaped holes corresponding to a membrane tension of ~0.05 mN/m, which is comparable to our previous calculation of the resting tension in the nuclear membranes that explains the separation between these membranes (Torbati *et al.*, 2016). At a lower resting tension of ~ 0.01 mN/m, the hole diameter is predicted to be ~ 240 nm (figure S5A, bottom). One possibility is that the lower stress pulses (Table 2) do not significantly perturb the resting tension in the nuclear membranes, while the higher force pulses result in a larger loss of the resting tension, resulting in bigger hole sizes.

The above model is limited in that it only accounts for the intiation of pore formation, and not the subsequent recruitment of membrane repair machinery like the ESCRT proteins that occurs over minutes (Denais *et al.*, 2016). These proteins can also apply physical forces onto the membranes (Chiaruttini *et al.*, 2015), change the geometry of the membranes and participating in resealing the hole. Further, hole

establishment may be a process that is far-from-equilibrium, and may be far more complex due to the many interactions between membrane embedded proteins, the nuclear lamina and the cellular cytoskeleton (Lele *et al.*, 2018).

Our experimental results show that the direct force probe can be an effective tool to engineer ruptures in the nuclear membranes in adherent cells. Application of precise and known levels of stress to the nucleus allows comparisons of rupture behavior across cell types and across different types of perturbations to nuclear membranes. This probe could be valuable in understanding if and how membrane components like LINC complex proteins that span the nuclear membranes, nuclear membrane composition and membrane-embedded proteins could contribute to nuclear membrane integrity under tensile forces.

Materials and Methods

Cell culture: All cell types were maintained at 37°C in a humidified 5% CO2 environment. Human breast epithelial cells (MCF-10A) were cultured in DMEM/F12 supplemented with 20 ng/ml EGF, 0.5 mg/ml hydrocortisone, 100 ng/ml cholera toxin, 100 μg/ml insulin and 5% horse serum (Debnath *et al.*, 2003). Human breast cancer cells (MDA-MB-231) and mouse embryonic fibroblasts (MEF) cells were cultured in 4.5 g/L glucose Dulbecco's modified Eagle's medium (DMEM) supplemented with 10% DBS and 1% penicillin-streptomycin.

Plasmid transfection: Transient transfection of plasmids into cells was performed with Lipofectamine 3000 reagent (Life Technologies/Invitrogen, Carlsbad, CA) in OPTI-MEM media (Life Technologies/Invitrogen, Carlsbad, CA). EGFP-NLS was a kind gift of Alexander Ishov at the University of Florida (Negorev *et al.*, 2001). Transfected cells were trypsinized and plated on to fibronectin-coated glass-bottomed dishes for micromanipulation and microscopy. The construction of cGAS-mCherry

(pCDH-CMV-cGASE225A/D227A-mCherry2-EF1- blastiS) was described previously (Civril *et al.*, 2013).

Immunostaining: Cells were fixed in 4% paraformaldehyde for 10 min, washed with PBS and then permeabilized and blocked with 0.1% triton X-100 in 1% bovine serum albumin (BSA) solution for 45 min. The primary antibodies used in this study included rabbit anti Lamin B2 (Abcam, used at 1:500) and mouse anti lamin A (Abcam, used at 1:1000). Cells were incubated with the primary antibody at 4 ºC overnight and secondary antibodies at room temperature for 1 h. Secondary antibodies used included goat anti-mouse Alexa Fluor 647 (Invitrogen, 1:500) and goat anti-rabbit Alexa Fluor 594 (Invitrogen, 1:500).

Micromanipulation: Micromanipulation was performed using an Eppendorf InjectMan micromanipulator system as described previously (Neelam et al., 2015; Zhang et al., 2018). In brief, a Femtotip micropipette tip (Eppendorf, 0.5 µm tip diameter) was mounted and connected to the Eppendorf microinjection system (InjectMan) by a tube. The cell membrane was penetrated with the micropipette tip, and the tip was brought next to the nuclear surface. The tube was then disconnected and opened to the atmosphere, which creates a known negative pressure which seals the micropipette tip to the ONM with a specified suction pressure (Neelam *et al.*, 2015; Zhang *et al.*, 2018). Nuclear deformation occured when the pipette was translated away from the nucleus. When the resistance to nuclear motion and deformation balanced the applied suction force, there was a subsequent release from the tip (this process occured in less than a second, resulting in a short stress pulse). The resisting stress on the ONM then is the suction stress at this point of detachment (calculated as suction pressure x area of tip). We have previously shown that the extent of nuclear motion and deformation depends on the suction force, and is not due to non-specific adhesion between the pipette tip and the membrane. Also we have calculated negligible pressure drop due to flow through nuclear pores, such that the stress on the ONM is, for practical purposes, identical to the suction pressure (Neelam *et al.*, 2015; Zhang *et al.*, 2018). Time lapse imaging was performed on a Nikon

TE 2000 inverted microscope with a 60× oil immersion objective and CCD camera (CoolSNAP, Photometrics, Tucson, AZ). Cells were maintained at 37°C, at 5% CO2 level throughout imaging.

siRNA transfection: The siGENOME SMARTpool siRNA targeting *LMNA* and *LMNB2* (Dharmacon) were used to deplete Lamin A and Lamin B2 proteins, respectively. The efficiency of siRNA depletion was confirmed by comparing the fluorescent intensity (confocal images, taken with the same imaging settings between scrambled group and transfected group) and the relative expression mRNA levels quantified with RT-qPCR (Figure S3D). To perform RT-qPCR, whole cells were lysed 72 hours post-transfection using the SingleShot Probes One-Step Kit (BioRad). Lysates were then combined with complete RT-qPCR reaction mix per the manufacturer's protocol, and pre-designed fluorogenic probes targeting either *LMNA*, *LMNB2*, or *GAPDH* (BioRad). Reactions were processed on a CFX-96 Real-time PCR detection system (BioRad) using the following thermocycler conditions: 10 minutes at 50˚C, 3 minutes at 95˚C, followed by 40 cycles of 15 seconds at 95˚C and 30 seconds at 60˚C. All results were analyzed using the 2-ΔΔCt method and normalized against *GAPDH* expression and a scrambled siRNA negative control (Livak and Schmittgen, 2001).

Analysis: NLS intensity of forced nuclei was normalized by the intensity of reference unforced nuclei in the same image to account for photo-bleaching effects as follows:

$$I_{t,n} = \frac{I_t / I_{t=0}}{I_{t,u} / I_{t=0,u}} \qquad (1)$$

where $I_{t,n}$ is the normalized intensity at time t, I_t is the fluorescence intensity of the stressed nucleus and $I_{t,u}$ is the fluorescence intensity of the unstressed nucleus quantified from images. The fractional loss of NLS intensity was calculated as 1-$I_{t=120,n}$ corresponding to t = 120 s. The initial rate of loss of NLS intensity in the nucleus was estimated by fitting the normalized intensity data for the first 20 s with a 5th order polynomial and then calculating the derivative by differentiating the polynomial and calculating the maximum rate. The area strain calculation was previously described in (Neelam *et al.*, 2015). Briefly, the

nucleus at its maximum deformation was overlaid onto its unstressed shape and the non-overlapping area calculated. The area strain was calculated as the non-overlapping area divided by the unstressed nuclear area.

Modeling:

Finite element calculations of diffusion from a hole in the surface of the flat cylindrical nucleus into the flat cylindrical cytoplasm were performed in COMSOL. Zero flux boundary conditions were imposed everywhere else except at the hole where continuity of concentration and mass flux was imposed. Predicted concentration in the nucleus was numerically averaged over the nuclear volume and normalized to the initial concentration. Initial rates were calculated from the time-dependent concentration profile in MATLAB by by first fitting a polynomial to the time dependent curve and differentiating this polynomial to calculate the initial rate. Next, hole size was varied, and initial rate dependence on hole size was calculated.

For mechanical calculations, the geometry of the membranes was modeled around a single donut-shaped pore as 2D elastic sheets with the Helfrich-Canham relation:

$$W = kH^2 + \bar{k}K \qquad (2)$$

where *H* is the mean curvature, *K* is the Gaussian curvature and $(k, \bar{k})$ are the bending moduli. The membranes were assumed to possess axisymmetry and reflection symmetry about the equatorial plane and hence, the geometry of only a single bilayer was simulated. The system is defined by the arclength *s*, the radial distance from the axis of revolution *r(s)*, the elevation from a base plane *z(s)* and the angle which the tangent makes with the radial vector ψ(s) (see Figure S5B). These parameters satisfy the geometric relations

$$r'(s) = \cos\psi \qquad (3)$$

$$z'(s) = \sin\psi \qquad (4)$$

$$\psi' = 2H - \sin\psi\,/r \qquad (5)$$

Here $()'$ is the partial derivative with respect to the arclength. These equations were integrated along with the force equilibrium equation, commonly referred to as the shape equation,

$$k\Delta H + 2kH(2H^2 - K) - 2kH^3 = 2\lambda H \qquad (6)$$

to compute the hole geometry. Here λ is the surface tension, Δ is the surface Laplacian and the transmembrane pressure was assumed to be zero. The integration was carried out with the following boundary conditions prescribed at the two ends of the simulated domain. The inner boundary is defined at the point where the membrane meets the equatorial plane at the hole site. Here we require z=0, ψ=π/2, and rH^'=0. The last boundary condition imposes zero transverse shear, a condition that arises from reflection symmetry present in the geometry and allows the membranes to slide freely at the equatorial plane.The far boundary is assumed to lie at a distance of 200 nm from the centre of the hole, midway between two typical adjacent holes (Belgareh and Doye, 1997; D'Angelo *et al.*, 2006; Dultz and Ellenberg, 2010). Here we require $\psi = 0$ and $\lambda = \lambda_0$, where $\lambda_0$is the prescribed resting tension in the membranes. In addition, we assume that no membrane is lost during the process of hole creation and expansion. We therefore simulate different hole diameters with a conserved membrane area. We implemented this constraint by switching from the independent variable from the arclength (s) to the surface area (a) and use the geometric relation $da = 2\pi rs\,ds$ to obtain the modified set of equations(Agrawal and Steigmann, 2009). We used the MATLAB solver BVP4C to perform numerical integration and computed the membrane geometry for different resting tensions.

Acknowledgments: This work was supported by awards from the National Institutes of Health [R01 EB014869 (T.P.L.); R01 HL082792 (J.L.) and U54 CA210184 (J.L) and the Department of Defense Breast Cancer Research Program [Breakthrough Award BC150580 (J.L)]. We thank Guanri Li for his assistance in imaging acquisition and data analysis.

References

Agrawal, A., and Steigmann, D. (2009). Boundary-value problems in the theory of lipid membranes. Continuum Mechanics and Thermodynamics *21*, 57-82.

Akimov, S.A., Volynsky, P.E., Galimzyanov, T.R., Kuzmin, P.I., Pavlov, K.V., and Batishchev, O.V. (2017a). Pore formation in lipid membrane I: Continuous reversible trajectory from intact bilayer through hydrophobic defect to transversal pore. Sci Rep *7*, 12152.

Akimov, S.A., Volynsky, P.E., Galimzyanov, T.R., Kuzmin, P.I., Pavlov, K.V., and Batishchev, O.V. (2017b). Pore formation in lipid membrane II: Energy landscape under external stress. Sci Rep *7*, 12509.

Alam, S.G., Lovett, D., Kim, D.I., Roux, K., Dickinson, R.B., and Lele, T.P. (2015). The nucleus is an intracellular propagator of tensile forces in NIH 3T3 fibroblasts. J Cell Sci *128*, 1901-1911.

Bakhoum, S.F., Ngo, B., Laughney, A.M., Cavallo, J.A., Murphy, C.J., Ly, P., Shah, P., Sriram, R.K., Watkins, T.B.K., Taunk, N.K., Duran, M., Pauli, C., Shaw, C., Chadalavada, K., Rajasekhar, V.K., Genovese, G., Venkatesan, S., Birkbak, N.J., McGranahan, N., Lundquist, M., LaPlant, Q., Healey, J.H., Elemento, O., Chung, C.H., Lee, N.Y., Imielenski, M., Nanjangud, G., Pe'er, D., Cleveland, D.W., Powell, S.N., Lammerding, J., Swanton, C., and Cantley, L.C. (2018). Chromosomal instability drives metastasis through a cytosolic DNA response. Nature *553*, 467-472.

Belgareh, N., and Doye, V. (1997). Dynamics of nuclear pore distribution in nucleoporin mutant yeast cells. J Cell Biol *136*, 747-759.

Broers, J.L., Peeters, E.A., Kuijpers, H.J., Endert, J., Bouten, C.V., Oomens, C.W., Baaijens, F.P., and Ramaekers, F.C. (2004). Decreased mechanical stiffness in LMNA-/- cells is caused by defective nucleo-cytoskeletal integrity: implications for the development of laminopathies. Hum Mol Genet *13*, 2567-2580.

Chancellor, T.J., Lee, J., Thodeti, C.K., and Lele, T. (2010). Actomyosin tension exerted on the nucleus through nesprin-1 connections influences endothelial cell adhesion, migration, and cyclic strain-induced reorientation. Biophys J *99*, 115-123.

Chang, W., Worman, H.J., and Gundersen, G.G. (2015). Accessorizing and anchoring the LINC complex for multifunctionality. J Cell Biol *208*, 11-22.

Chiaruttini, N., Redondo-Morata, L., Colom, A., Humbert, F., Lenz, M., Scheuring, S., and Roux, A. (2015). Relaxation of Loaded ESCRT-III Spiral Springs Drives Membrane Deformation. Cell *163*, 866-879.

Civril, F., Deimling, T., de Oliveira Mann, C.C., Ablasser, A., Moldt, M., Witte, G., Hornung, V., and Hopfner, K.P. (2013). Structural mechanism of cytosolic DNA sensing by cGAS. Nature *498*, 332-337.

D'Angelo, M.A., Anderson, D.J., Richard, E., and Hetzer, M.W. (2006). Nuclear pores form de novo from both sides of the nuclear envelope. Science *312*, 440-443.

Dahl, K.N., Ribeiro, A.J., and Lammerding, J. (2008). Nuclear shape, mechanics, and mechanotransduction. Circ Res *102*, 1307-1318.

Davidson, P.M., Sliz, J., Isermann, P., Denais, C., and Lammerding, J. (2015). Design of a microfluidic device to quantify dynamic intra-nuclear deformation during cell migration through confining environments. Integr Biol (Camb) *7*, 1534-1546.

Debnath, J., Muthuswamy, S.K., and Brugge, J.S. (2003). Morphogenesis and oncogenesis of MCF-10A mammary epithelial acini grown in three-dimensional basement membrane cultures. Methods *30*, 256-268.

Denais, C.M., Gilbert, R.M., Isermann, P., McGregor, A.L., te Lindert, M., Weigelin, B., Davidson, P.M., Friedl, P., Wolf, K., and Lammerding, J. (2016). Nuclear envelope rupture and repair during cancer cell migration. Science *352*, 353-358.

Deviri, D., Discher, D.E., and Safran, S.A. (2017). Rupture Dynamics and Chromatin Herniation in Deformed Nuclei. Biophys J *113*, 1060-1071.

Dultz, E., and Ellenberg, J. (2010). Live imaging of single nuclear pores reveals unique assembly kinetics and mechanism in interphase. J Cell Biol *191*, 15-22.

Foisner, R. (2001). Inner nuclear membrane proteins and the nuclear lamina. J Cell Sci *114*, 3791-3792.

Gonzalez-Rodriguez, D., Maddugoda, M.P., Stefani, C., Janel, S., Lafont, F., Cuvelier, D., Lemichez, E., and Brochard-Wyart, F. (2012). Cellular dewetting: opening of macroapertures in endothelial cells. Phys Rev Lett *108*, 218105.
Hatch, E.M., Fischer, A.H., Deerinck, T.J., and Hetzer, M.W. (2013). Catastrophic nuclear envelope collapse in cancer cell micronuclei. Cell *154*, 47-60.
Hatch, E.M., and Hetzer, M.W. (2016). Nuclear envelope rupture is induced by actin-based nucleus confinement. J Cell Biol *215*, 27-36.
Irianto, J., Xia, Y., Pfeifer, C.R., Athirasala, A., Ji, J., Alvey, C., Tewari, M., Bennett, R.R., Harding, S.M., Liu, A.J., Greenberg, R.A., and Discher, D.E. (2017). DNA Damage Follows Repair Factor Depletion and Portends Genome Variation in Cancer Cells after Pore Migration. Current biology : CB *27*, 210-223.
Isermann, P., and Lammerding, J. (2013). Nuclear mechanics and mechanotransduction in health and disease. Curr Biol *23*, R1113-1121.
Kirby, T.J., and Lammerding, J. (2018). Emerging views of the nucleus as a cellular mechanosensor. Nat Cell Biol *20*, 373-381.
Lammerding, J., Fong, L.G., Ji, J.Y., Reue, K., Stewart, C.L., Young, S.G., and Lee, R.T. (2006). Lamins A and C but not lamin B1 regulate nuclear mechanics. J Biol Chem *281*, 25768-25780.
Lammerding, J., Hsiao, J., Schulze, P.C., Kozlov, S., Stewart, C.L., and Lee, R.T. (2005). Abnormal nuclear shape and impaired mechanotransduction in emerin-deficient cells. J Cell Biol *170*, 781-791.
Lammerding, J., and Lee, R.T. (2009). Mechanical properties of interphase nuclei probed by cellular strain application. Methods Mol Biol *464*, 13-26.
Lammerding, J., Schulze, P.C., Takahashi, T., Kozlov, S., Sullivan, T., Kamm, R.D., Stewart, C.L., and Lee, R.T. (2004). Lamin A/C deficiency causes defective nuclear mechanics and mechanotransduction. J Clin Invest *113*, 370-378.
Lammerding, J., and Wolf, K. (2016). Nuclear envelope rupture: Actin fibers are putting the squeeze on the nucleus. J Cell Biol *215*, 5-8.
Lee, Y.L., and Burke, B. (2018). LINC complexes and nuclear positioning. Semin Cell Dev Biol *82*, 67-76.
Lele, T.P., Dickinson, R.B., and Gundersen, G.G. (2018). Mechanical principles of nuclear shaping and positioning. J Cell Biol.
Livak, K.J., and Schmittgen, T.D. (2001). Analysis of relative gene expression data using real-time quantitative PCR and the 2(-Delta Delta C(T)) Method. Methods *25*, 402-408.
Luxton, G.W., and Starr, D.A. (2014). KASHing up with the nucleus: novel functional roles of KASH proteins at the cytoplasmic surface of the nucleus. Curr Opin Cell Biol *28*, 69-75.
Maniotis, A.J., Chen, C.S., and Ingber, D.E. (1997). Demonstration of mechanical connections between integrins, cytoskeletal filaments, and nucleoplasm that stabilize nuclear structure. Proc Natl Acad Sci U S A *94*, 849-854.
Neelam, S., Chancellor, T.J., Li, Y., Nickerson, J.A., Roux, K.J., Dickinson, R.B., and Lele, T.P. (2015). Direct force probe reveals the mechanics of nuclear homeostasis in the mammalian cell. Proc Natl Acad Sci U S A *112*, 5720-5725.
Neelam, S., Hayes, P.R., Zhang, Q., Dickinson, R.B., and Lele, T.P. (2016). Vertical uniformity of cells and nuclei in epithelial monolayers. Sci Rep *6*, 19689.
Negorev, D., Ishov, A.M., and Maul, G.G. (2001). Evidence for separate ND10-binding and homo-oligomerization domains of Sp100. J Cell Sci *114*, 59-68.
Pajerowski, J.D., Dahl, K.N., Zhong, F.L., Sammak, P.J., and Discher, D.E. (2007). Physical plasticity of the nucleus in stem cell differentiation. Proc Natl Acad Sci U S A *104*, 15619-15624.
Raab, M., Gentili, M., de Belly, H., Thiam, H.R., Vargas, P., Jimenez, A.J., Lautenschlaeger, F., Voituriez, R., Lennon-Duménil, A.M., Manel, N., and Piel, M. (2016). ESCRT III repairs nuclear envelope ruptures during cell migration to limit DNA damage and cell death. Science *352*, 359-362.
Schäpe, J., Prausse, S., Radmacher, M., and Stick, R. (2009). Influence of lamin A on the mechanical properties of amphibian oocyte nuclei measured by atomic force microscopy. Biophys J *96*, 4319-4325.

Staykova, M., Holmes, D.P., Read, C., and Stone, H.A. (2011). Mechanics of surface area regulation in cells examined with confined lipid membranes. Proc Natl Acad Sci U S A *108*, 9084-9088.
Stephens, A.D., Banigan, E.J., Adam, S.A., Goldman, R.D., and Marko, J.F. (2017). Chromatin and lamin A determine two different mechanical response regimes of the cell nucleus. Mol Biol Cell *28*, 1984-1996.
Swift, J., Ivanovska, I.L., Buxboim, A., Harada, T., Dingal, P.C., Pinter, J., Pajerowski, J.D., Spinler, K.R., Shin, J.W., Tewari, M., Rehfeldt, F., Speicher, D.W., and Discher, D.E. (2013). Nuclear lamin-A scales with tissue stiffness and enhances matrix-directed differentiation. Science *341*, 1240104.
Tajik, A., Zhang, Y., Wei, F., Sun, J., Jia, Q., Zhou, W., Singh, R., Khanna, N., Belmont, A.S., and Wang, N. (2016). Transcription upregulation via force-induced direct stretching of chromatin. Nat Mater.
Torbati, M., Lele, T.P., and Agrawal, A. (2016). Ultradonut topology of the nuclear envelope. Proc Natl Acad Sci U S A *113*, 11094-11099.
Uhler, C., and Shivashankar, G.V. (2017). Regulation of genome organization and gene expression by nuclear mechanotransduction. Nat Rev Mol Cell Biol *18*, 717-727.
Wang, N., Tytell, J.D., and Ingber, D.E. (2009). Mechanotransduction at a distance: mechanically coupling the extracellular matrix with the nucleus. Nat Rev Mol Cell Biol *10*, 75-82.
Wolf, K., Te Lindert, M., Krause, M., Alexander, S., Te Riet, J., Willis, A.L., Hoffman, R.M., Figdor, C.G., Weiss, S.J., and Friedl, P. (2013). Physical limits of cell migration: control by ECM space and nuclear deformation and tuning by proteolysis and traction force. J Cell Biol *201*, 1069-1084.
Wu, J., Corbett, A.H., and Berland, K.M. (2009). The intracellular mobility of nuclear import receptors and NLS cargoes. Biophys J *96*, 3840-3849.
Wu, J., Kent, I.A., Shekhar, N., Chancellor, T.J., Mendonca, A., Dickinson, R.B., and Lele, T.P. (2014). Actomyosin pulls to advance the nucleus in a migrating tissue cell. Biophys J *106*, 7-15.
Zhang, Q., Tamashunas, A.C., and Lele, T.P. (2018). A Direct Force Probe for Measuring Mechanical Integration Between the Nucleus and the Cytoskeleton. J Vis Exp.

Table 1. Parameters used for finite element analysis in Figure 4.

	Nucleus	Cell		Nucleus	Cytoplasm
Height	4.2 μm	4.2 μm	Diffusion coefficient	19 μm²/s	14 μm²/s
Radius	8.6 μm	20 μm	Initial Intensity	1	0.3

Table 2. Comparison between experimental and simulation data

Simulation		Experimental		
Initial Rate (/s) ×1000	Hole Size (nm)	Stress (kPa)	Initial Rate (/s) ×1000	Hole Size (nm)
-1.00	80	2	- 1.45 ± 0.16	115 ± 14
-1.27	100	5	-1.21 ± 0.22	96 ± 17
-1.50	120	8	-1.96 ± 0.36	156 ± 27
-1.76	140	10	-5.62 ± 1.50	450 ± 119
-2.02	160	30	-5.50 ± 0.94	465 ± 72
-5.50	440			
-5.76	460			

Left column shows initial rates of decrease in EGFP-NLS concentration in the nucleus calculated from the finite element analysis in Figure 4, for different hole sizes (diameter). The magnitude of the rate increases for increasing hole size as expected. Right column shows initial rates (i.e. immediately after the stress pulse) estimated from experimental plots of EGFP-NLS intensity in the nucleus with time. Comparison with simulations was used to estimate the hole size which is shown in the rightmost column.

Figure 1. Local tensile stress applied to the nucleus in adherent cells can rupture the nuclear membranes. A. Top: images shows a representative MCF-10A nucleus expressing EGFP-NLS before application of stress (unstressed) and at the point of maximum deformation due to a local stress pulse of 10 kPa and duration of < 1 s. The arrow indicates the location where the micropipette tip was attached to the nucleus. Outline overlay compares the outlines of the unstressed and deformed nucleus (right). Bottom, inverted time lapse fluorescent images of the nucleus probed above along with cytoplasm. The images show that the cytoplasmic intensity increases and nuclear intensity decreases - the corresponding quantification of cytoplasmic and nuclear intensities (normalized to the corresponding initial intensity; stress pulse applied at time = 0) is shown in B - over the first several seconds, which indicates membrane rupture. Over longer times (~30 mins), both cytoplasmic and nuclear intensity are restored to levels before rupture indicating the nuclear membranes are repaired over time. C. Image shows mCherry- cGAS stably expressing MDA-MB-231 cell nucleus transfected with EGFP-NLS. Local tensile stress of 10 kPa (at the site indicated by rectangular box) causes the accumulation of cGAS cytoplasmic DNA binding protein near the site of stress application.

Figure 2. The extent of rupture of nuclear membranes scales with the magnitude of tensile stress. A. Plot shows pooled measurements of cytoplasmic and nuclear EGFP-NLS fluorescence intensities (normalized to the initial intensity) at 120 s after a stress pulse was applied to the MCF10A nucleus (grey and orange circles respectively), along with EGFP-NLS fluorescence intensities in nuclei (blue; normalized to the initial intensity) which were present in the same field of view as the stressed nucleus, but which were not subjected to stress. The decrease in the fluorescence intensity of unstressed nuclei is due to photobeaching during image capture. The fluorescence intensity of stressed nuclei decreases consistently after application of the stress pulse. Data was pooled from 23 nuclei. The stress applied was 10 kPa. Error bars are S.E.M.). Statistical differences were detected with two-way ANOVA (* represents $p < 0.05$). B. Plot shows pooled mean values of normalized EGFP-NLS intensity from at least 20 nuclei per stress magnitude. Normalization involved correcting for effects of photobleaching by dividing stressed nuclear EGFP-NLS intensities with EGFP-NLS intensities in the unstressed control nucleus in the same field of

view for each cell probed (see materials and methods for details on normalization). Rupture behavior is seen to change with the magnitude of stress applied. Error bars are S.E.M. (N≥20).). Statistical differences were detected with two-way ANOVA with Bonferonni correction (* represents $p <$ 0.05/number of comparison). C. Plot shows the fractional loss of nuclear EGFP-NLS intensity quantified from the data in B at 120 seconds after the stress pulse (see materials and methods for calculation). The data shows that the extent of NLS loss is larger at a higher magnitude of stress. Error bars are S.E.M. (N≥20).

Figure 3. Effect of lamin depletion on nuclear membrane rupture caused by local tensile stress. Plots show pooled mean normalized nuclear EGFP-NLS intensity after a 10 kPa stress pulse was applied to the nucleus in MCF-10A cells transfected with non-targeting siRNA (scrambled) and siRNA targeting *LMNA* (A) and (B) siRNA targeting *LMNB2* (N≥22 for each condition). Statistical differences were detected with ANOVA (* represents $p < 0.05$). C and D. Plots show the normalized nuclear EGFP-NLS intensity at 120 s after a 10 kPa stress pulse vs. the maximum nuclear deformation (quantified as area strain) in MCF-10A cells transfected with non-targeting siRNA or siRNA targeting *LMNB2* (C) and in MCF-10A cells transfected with non-targeting siRNA or siRNA targeting *LMNA* (D). Error bars are S.E.M (N≥21). The EGFP-NLS intensity at the pseudo-steady state of 120 s post rupture appears to correlate with the maximum deformation. E. Plots show the normalized nuclear EGFP-NLS intensity at 120 s post a stress pulse vs. the maximum nuclear deformation (quantified as area strain) in MCF-10A cells (blue symbols; square corresponds to 10 kPa and circle corresponds to 30 kPa), and MEFs (grey symbols; square corresponds to 10 kPa and circle corresponds to 30 kPa). Error bars are S.E.M (N≥17). For a given cell type, the pseudo-steady fluorescence intensity of EGFP-NLS at 120 s post-rupture scales inversely with the extent of deformation.

Figure 4. Experimental estimation of the hole size and prediction of donut hole sizes. A. X-Y views of a finite element calculation of nuclear EGFP-NLS diffusion from a hole in the nucleus (marked by an arrow). The nucleus and cell are modeled as flat cylinders with geometrical parameters taken from experimental measurements in (Neelam *et al.*, 2016) and nuclear and cytoplasmic diffusion coefficients

from (Wu *et al.*, 2009) (see Table 1). B. Initial rate of EGFP-NLS diffusion from the nucleus into the cytoplasm through nuclear hole as a function of hole size calculated from the finite element model in A (for details of how the initial rate was calculated from data, see materials and methods). C. shows experimental measurements of initial rate of nuclear EGFP-NLS decrease in the nucleus at different stress levels. Error bars are S.E.M. N≥22 for each stress.

Movie Legend:

Movie 1: Time-lapse movie showing the short duration of the 10 kPa stress pulse applied to an MCF-10A nucleus expressing EGFP-NLS (corresponding to Figure 1A).

Supplemental Figures:

Figure S1. A. Histograms of EGFP-NLS intensity normalized to initial intensity in unstressed (blue, Ref) and stressed nuclei (orange) at the indicated pressures, at 120 s after the stress pulse. N≥20 for each stress level. P_R shows the probability of rupture calculated as the fraction of samples that exhibited NLS intensity less than the mean reference intensity (i.e. of the unstressed nucleus) less the SEM. B. Histograms of EGFP-NLS intensity normalized to initial intensity in unstressed (blue, Ref), 10 kPa stressed lamin A/C depleted, lamin B2 depleted (orange) and scrambled siRNA transfected nuclei (black) 120 s after the stress pulse. N≥22 for each condition.

Figure S2. A. Plot shows the pooled normalized mean EGFP-NLS intensity at 10 kPa in MEF WT cells at 10 kPa and 30 kPa. Error bars are S.E.M (N≥17). Statistical differences were detected with two-way ANOVA (* represents $p < 0.05$). B. Plots show area strain of nuclear deformation in MEF WT cells. Error bars are S.E.M (N≥17). Statistical differences were detected with Student's T-test (* represents $p < 0.05$).

Figure S3. Validation of siRNA transfection. Fluorescent images show the MCF-10A cells transfected with scrambled (non-targeting) siRNA (top) and siRNA targeting *LMNA* (A) or *LMNB2* (B). C. Fluorescence intensity of indicated proteins in nuclei relative to control (scrambled siRNA transfected cells). siRNA transfection results in nearly 60% decrease in fluorescence intensity of the targeted protein. Student's T-test shows no statistical difference. D. Relative levels of mRNA transcripts measured by RT-qPCR showing a more than 80% decrease upon siRNA transfection for both lamin A/C and lamin B2. Student's T-test shows no statistical difference.

Figure S4. Plots show maximum nuclear deformation (quantified as area strain) under a 10 kPa stress pulse in MCF-10A cells transfected with scrambled siRNA or siRNA targeting lamin A/C and lamin B2. Error bars are S.E.M (N≥21). Area strain is higher in lamin A/C depleted cells but not lamin B2 depleted cells. Statistical differences were detected with Student's T-test (* represents $p < 0.05$).

Figure S5. A. Computation of membrane geometry for donut-shaped holes in the nuclear bilayers corresponding to a membrane tension of ~0.08 mN/m (top) and 0.002 mN/m (bottom). Lower tension corresponds to a larger hole diameter. B. Schematic of membrane geometry. r is the radial distance, z is the height, and ψ is the angle of the tangent vector with the radial direction.

Figure S6. Applying suction pressure to the nuclear envelope for several seconds does not cause leakage of EGFP-NLS into the micropipette. A. DIC image shows the micropipette tip attached to the nuclear surface. Suction was applied to the nucleus for 10.9 s without any measurable change in the nuclear EGFP-NLS intensity. At 10.9 s, the pipette was moved away, at which point the nucleus deformed. The deformation demonstrates that the micropipette tip in this experiment was indeed suction-sealed to the nuclear surface. Plot in B shows the corresponding quantification of fluorescence intensity (grey curve is intensity in the nucleus in A after suction was applied), and quantification of intensity in another nucleus (orange) in the field of view (not shown in A) that was not subjected to micromanipulation. Comparison of the orange and grey curves shows that the small decrease in EGFP-NLS intensity in the experiment in A is caused by photobleaching due to image capture. C. Pooled average of normalized fluorescence intensity (suction/unstressed) for 12 different nuclei. Suction was applied for ~ 5 s, which is a much longer time than the <1s time for which the nucleus was deformed in the rupture experiments. In each experiment, suction-sealing of the pipette to the nuclear surface was confirmed by moving the pipette away after 5 s and checking that the nucleus deformed. Error bar is standard deviation.

Figure 1

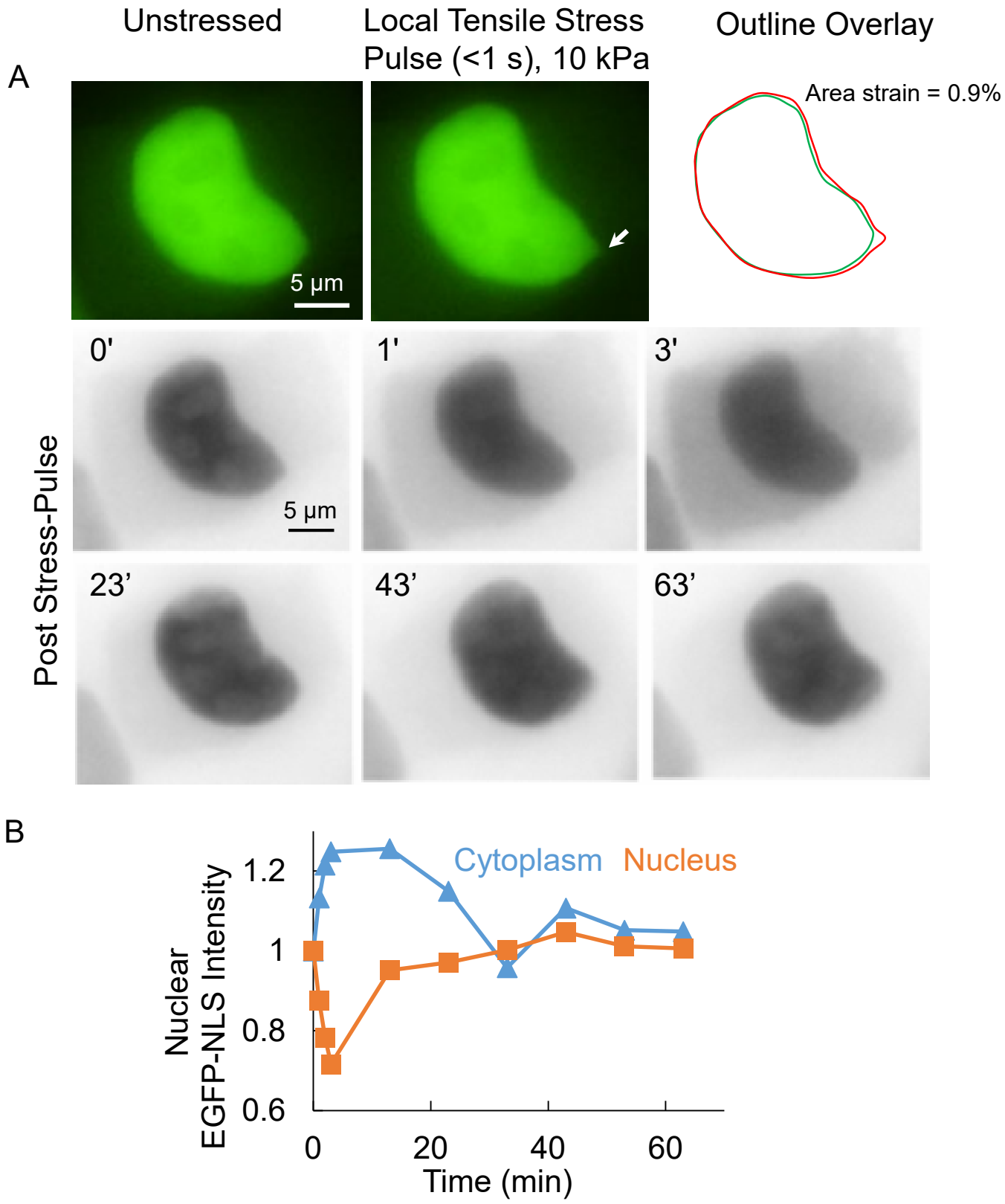
A
Unstressed
Local Tensile Stress Pulse (<1 s), 10 kPa
Outline Overlay
Area strain = 0.9%
5 μm
Post Stress-Pulse
0'
1'
3'
5 μm
23'
43'
63'
B
Cytoplasm
Nucleus
Nuclear EGFP-NLS Intensity
1.2
1
0.8
0.6
0
20
40
60
Time (min)

Figure 1

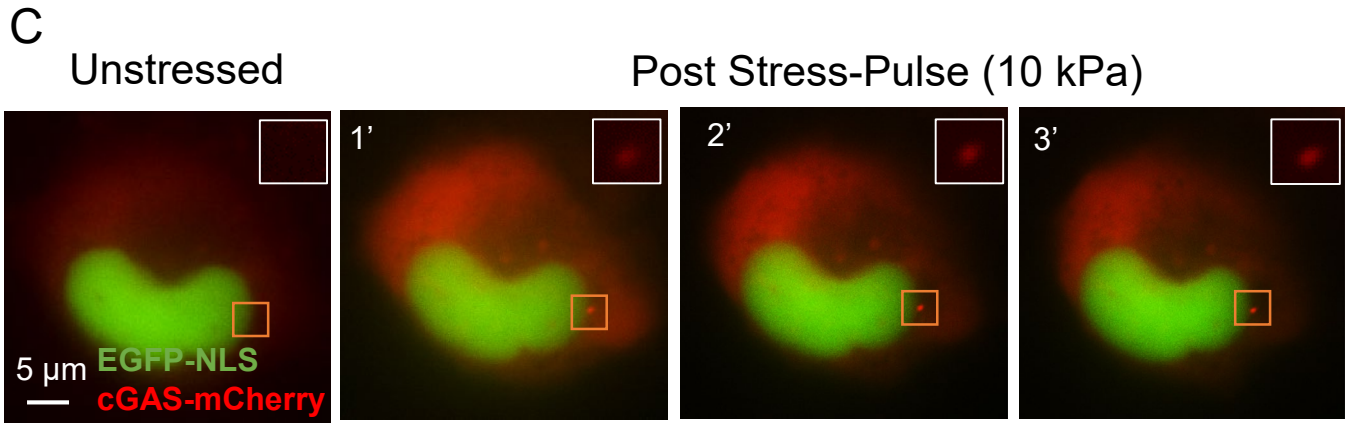
C
Unstressed
Post Stress-Pulse (10 kPa)
1'
2'
3'
5 µm
EGFP-NLS
cGAS-mCherry

Figure 2

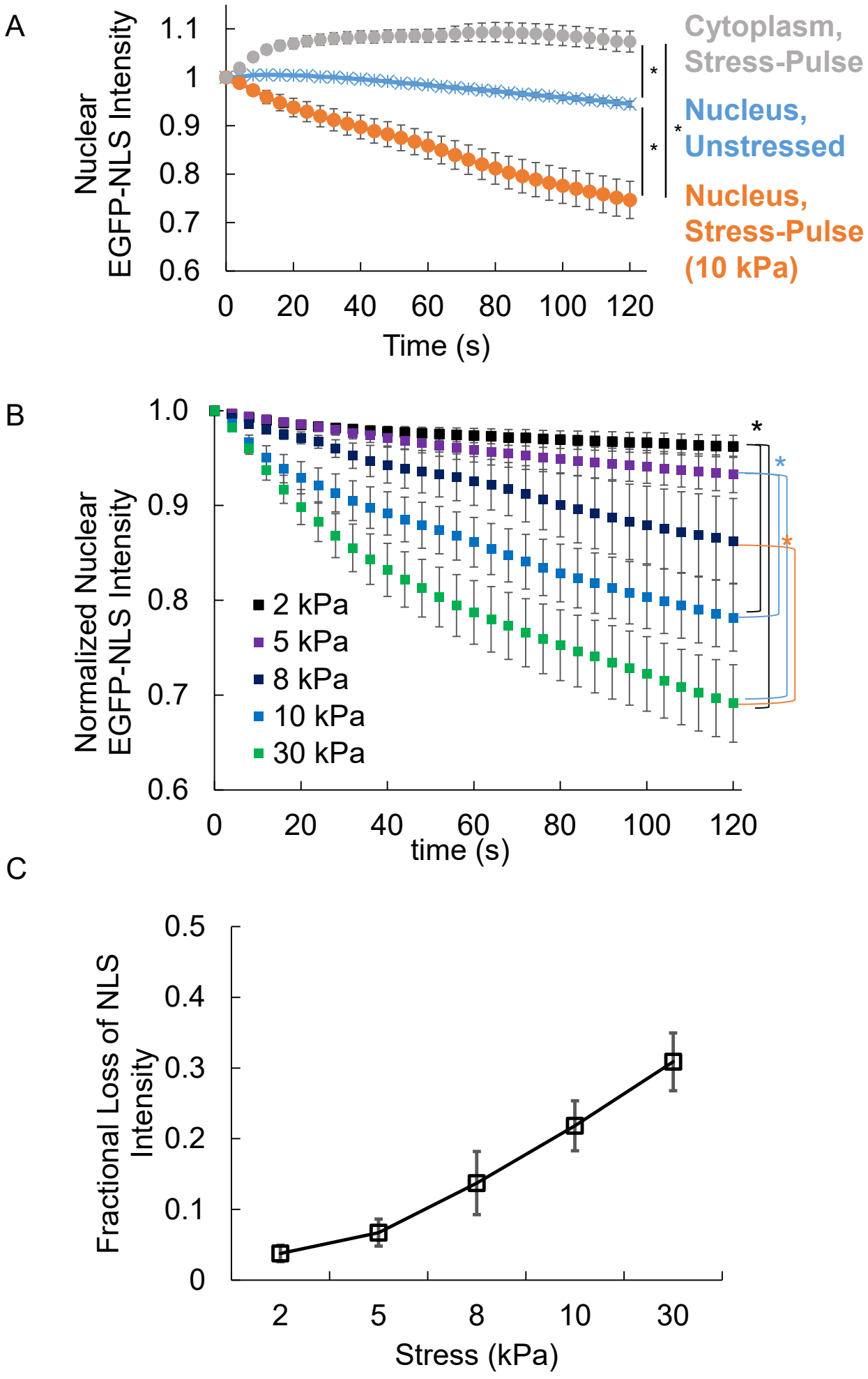
A
Nuclear EGFP-NLS Intensity
1.1
1
0.9
0.8
0.7
0.6
0
20
40
60
80
100
120
Time (s)
Cytoplasm, Stress-Pulse
Nucleus, Unstressed
Nucleus, Stress-Pulse (10 kPa)
*
*
*
B
Normalized Nuclear EGFP-NLS Intensity
1.0
0.9
0.8
0.7
0.6
2 kPa
5 kPa
8 kPa
10 kPa
30 kPa
0
20
40
60
80
100
120
time (s)
*
*
*
C
Fractional Loss of NLS Intensity
0.5
0.4
0.3
0.2
0.1
0
2
5
8
10
30
Stress (kPa)

Figure 3

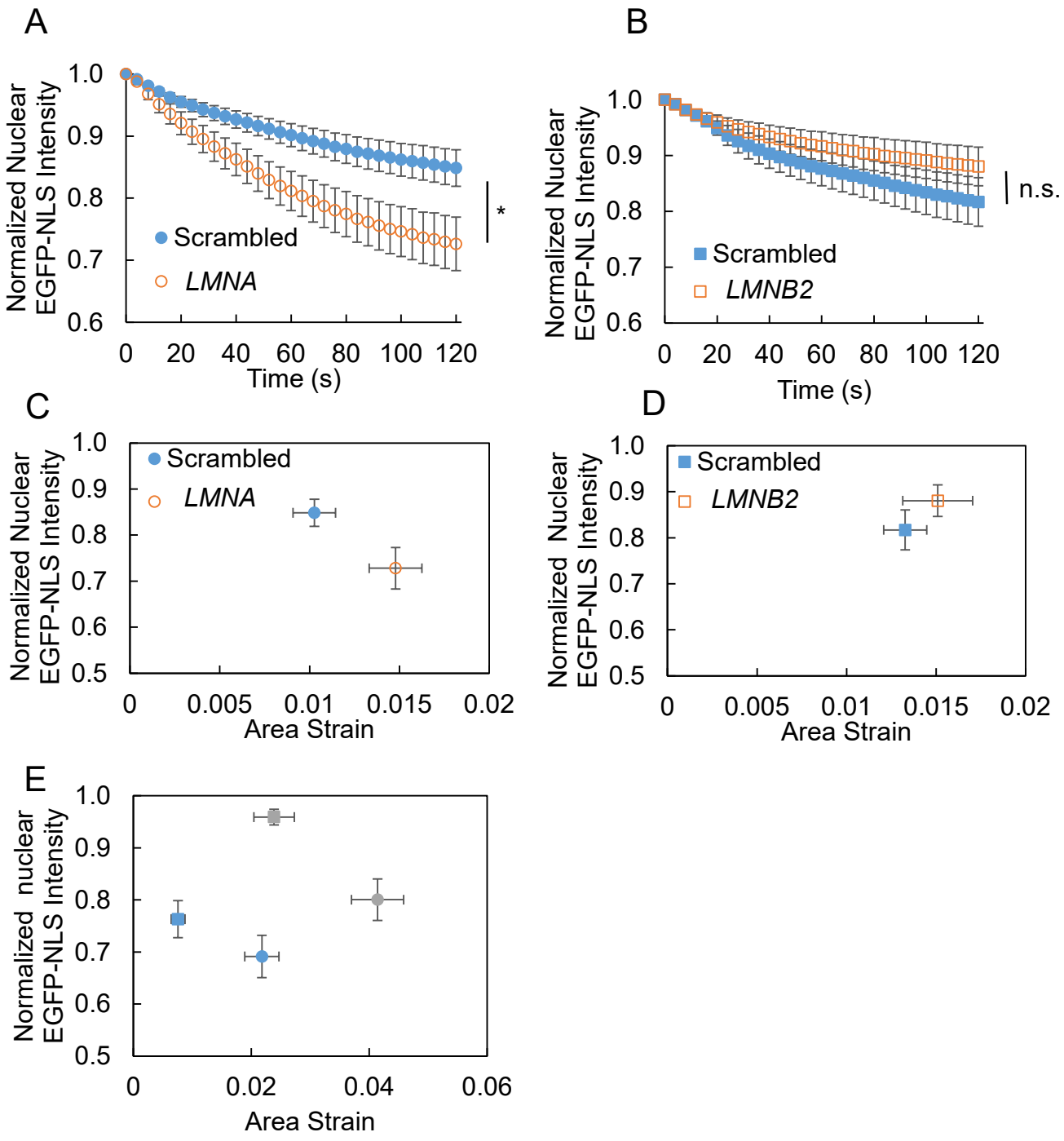
A
Normalized Nuclear EGFP-NLS Intensity
1.0
0.9
0.8
0.7
0.6
Scrambled
LMNA
*
0
20
40
60
80
100
120
Time (s)
B
Normalized Nuclear EGFP-NLS Intensity
1.0
0.9
0.8
0.7
0.6
Scrambled
LMNB2
n.s.
0
20
40
60
80
100
120
Time (s)
C
Normalized Nuclear EGFP-NLS Intensity
1.0
0.9
0.8
0.7
0.6
0.5
Scrambled
LMNA
0
0.005
0.01
0.015
0.02
Area Strain
D
Normalized Nuclear EGFP-NLS Intensity
1.0
0.9
0.8
0.7
0.6
0.5
Scrambled
LMNB2
0
0.005
0.01
0.015
0.02
Area Strain
E
Normalized nuclear EGFP-NLS Intensity
1.0
0.9
0.8
0.7
0.6
0.5
0
0.02
0.04
0.06
Area Strain

Figure 4

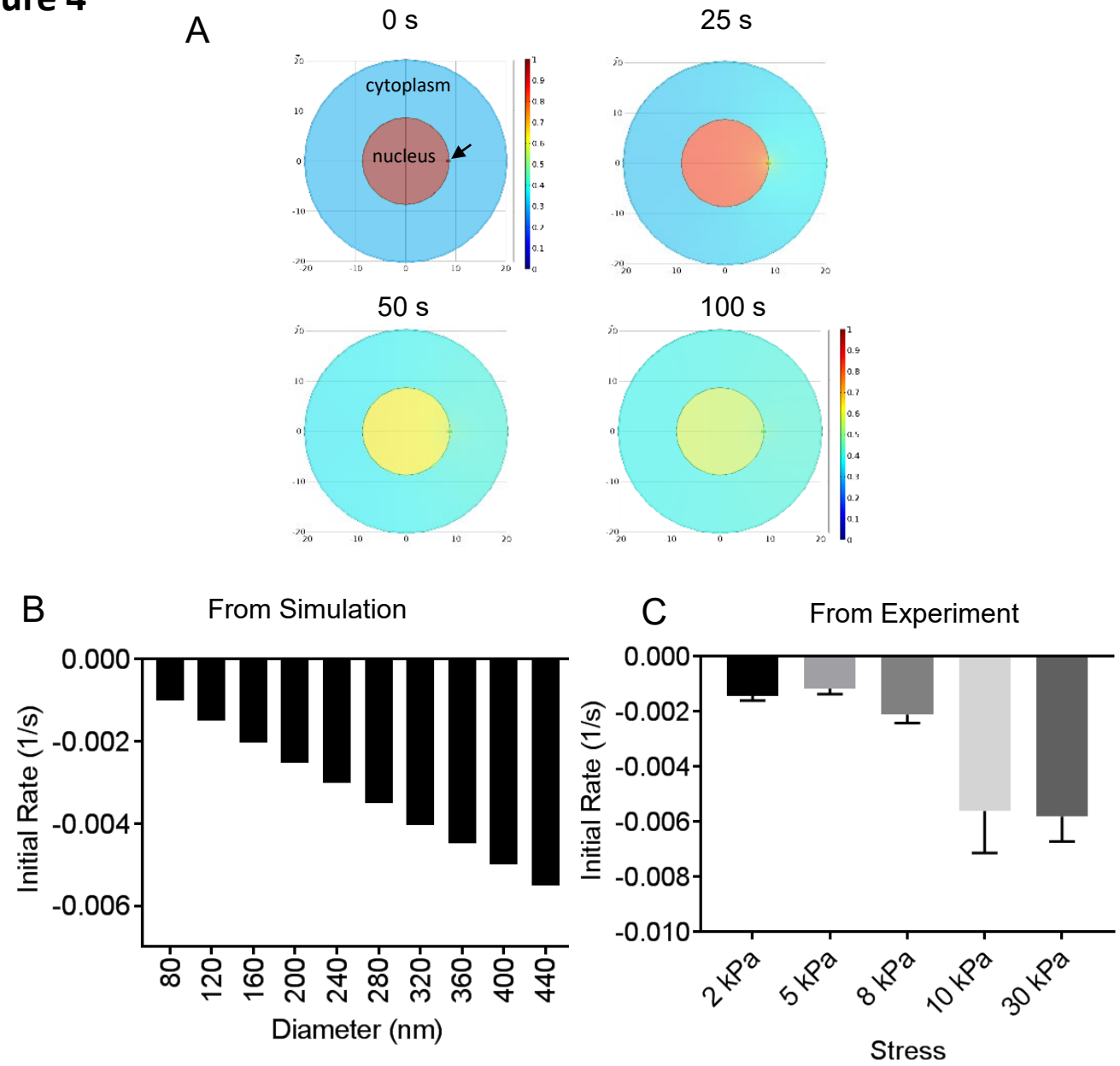
A
0 s
25 s
50 s
100 s
cytoplasm
nucleus
B
From Simulation
Initial Rate (1/s)
0.000
-0.002
-0.004
-0.006
80
120
160
200
240
280
320
360
400
440
Diameter (nm)
C
From Experiment
Initial Rate (1/s)
0.000
-0.002
-0.004
-0.006
-0.008
-0.010
2 kPa
5 kPa
8 kPa
10 kPa
30 kPa
Stress

Figure S1

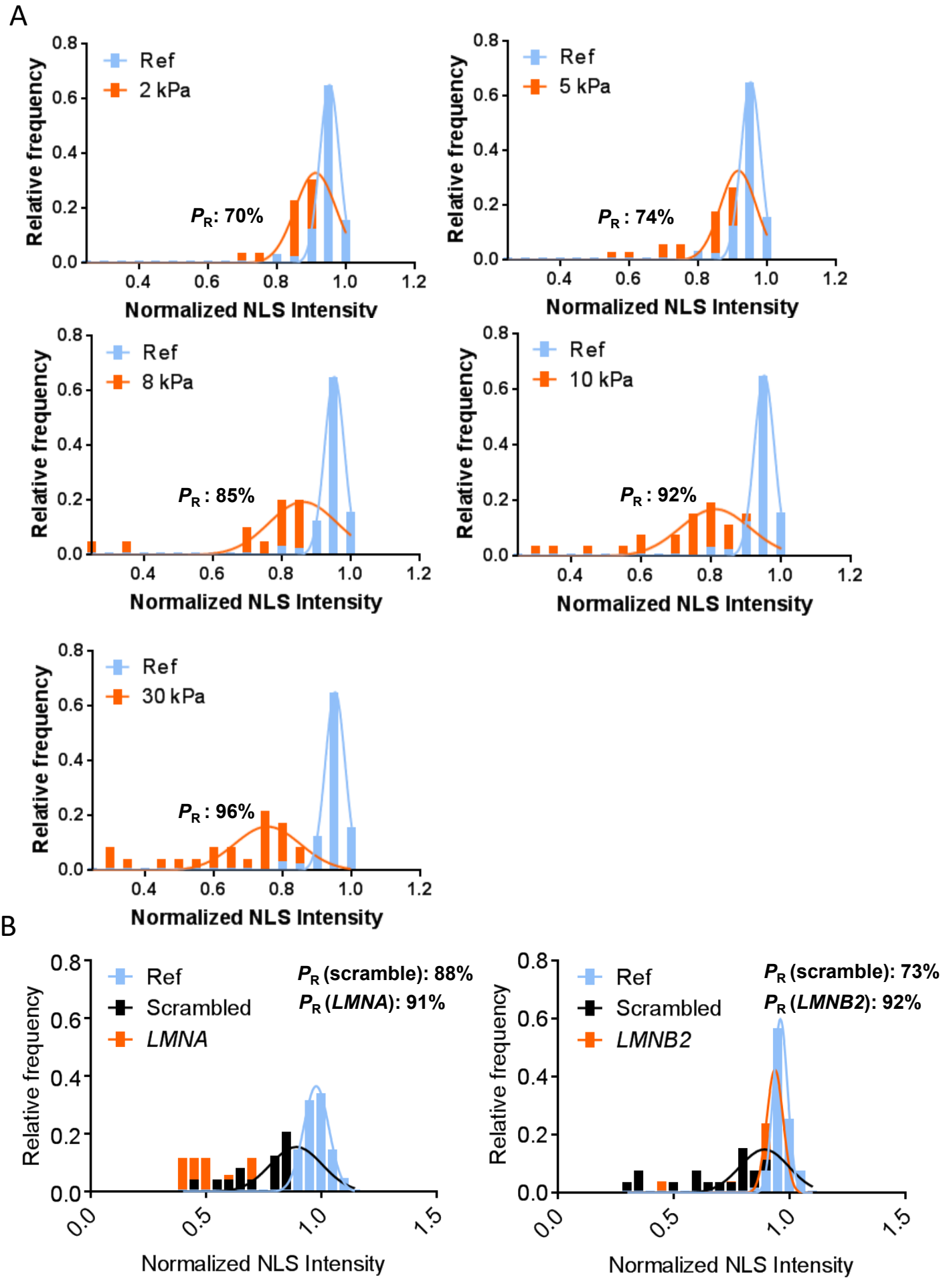
A
Ref
2 kPa
P_R: 70%
Relative frequency
Normalized NLS Intensity
Ref
5 kPa
P_R : 74%
Ref
8 kPa
P_R : 85%
Ref
10 kPa
P_R : 92%
Ref
30 kPa
P_R : 96%
B
Ref
Scrambled
LMNA
P_R (scramble): 88%
P_R (*LMNA*): 91%
Ref
Scrambled
LMNB2
P_R (scramble): 73%
P_R (*LMNB2*): 92%

Figure S2

A

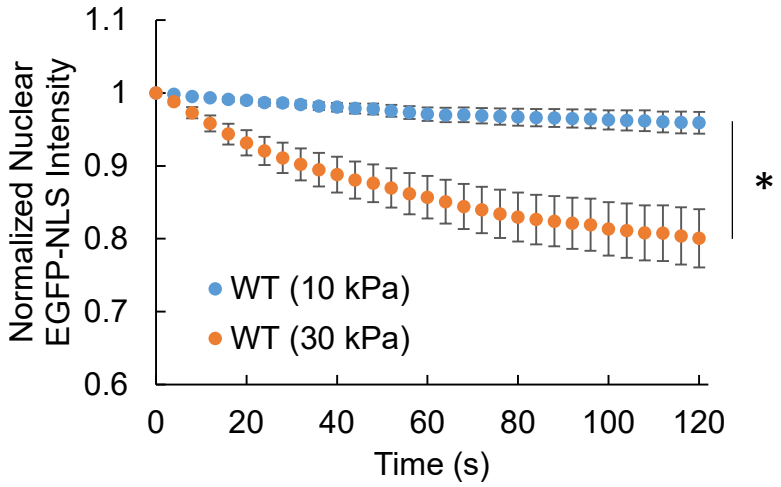
Normalized Nuclear EGFP-NLS Intensity
1.1
1
0.9
0.8
0.7
0.6
0
20
40
60
80
100
120
Time (s)
WT (10 kPa)
WT (30 kPa)
*

B

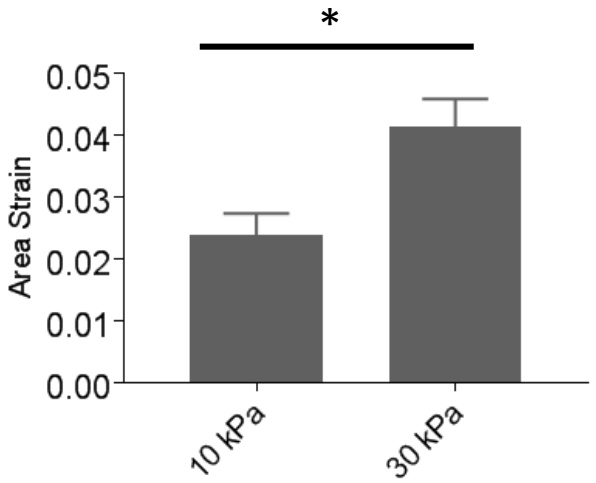
*
Area Strain
0.05
0.04
0.03
0.02
0.01
0.00
10 kPa
30 kPa

Figure S3

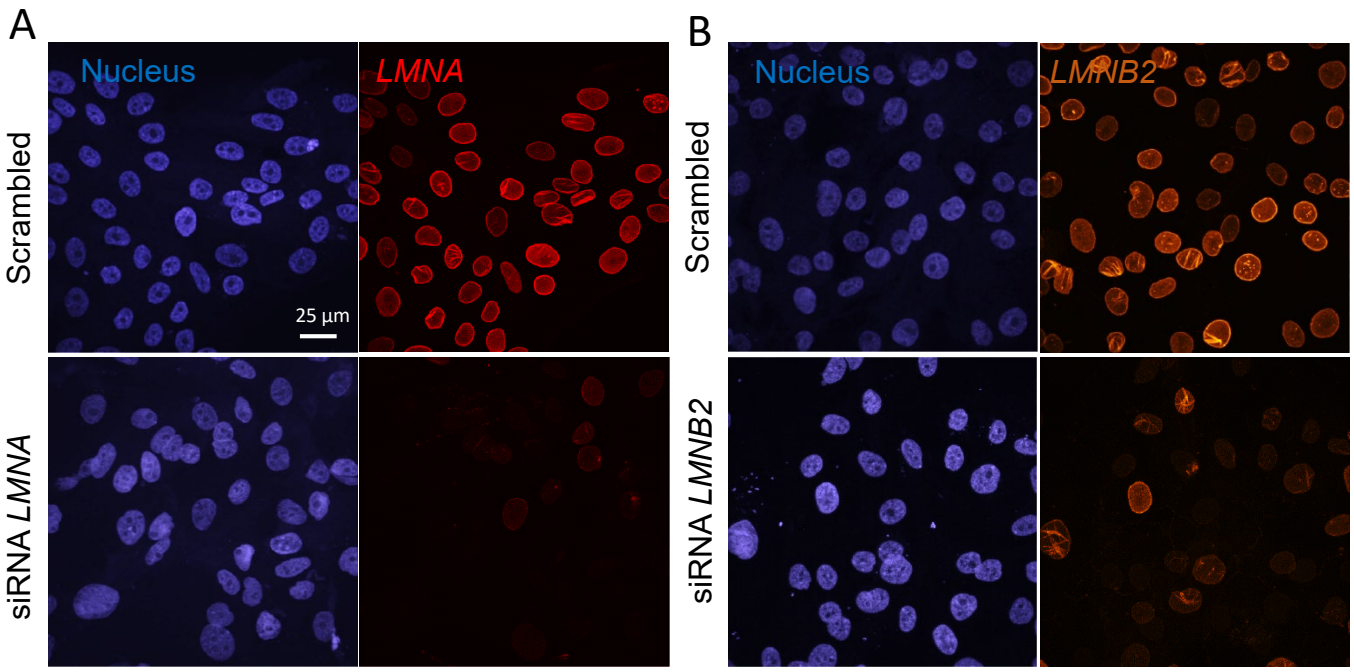
A
Nucleus
LMNA
Scrambled
siRNA LMNA
25 µm
B
Nucleus
LMNB2
Scrambled
siRNA LMNB2

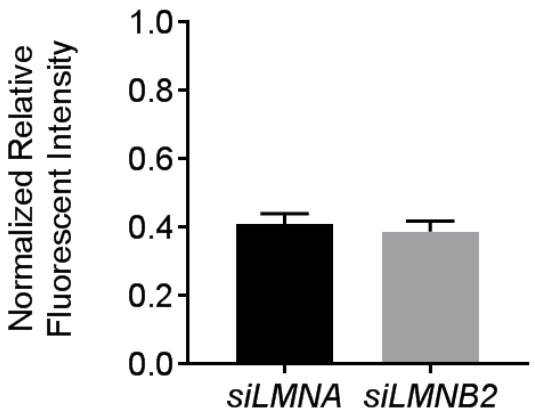
C
Normalized Relative Fluorescent Intensity
1.0
0.8
0.6
0.4
0.2
0.0
siLMNA
siLMNB2

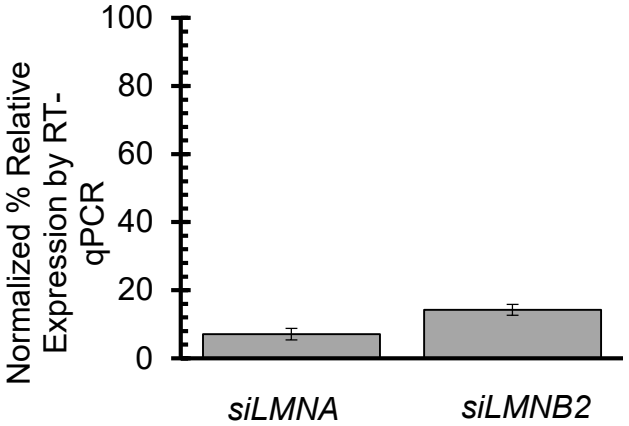
D
Normalized % Relative Expression by RT-qPCR
100
80
60
40
20
0
siLMNA
siLMNB2

Figure S4

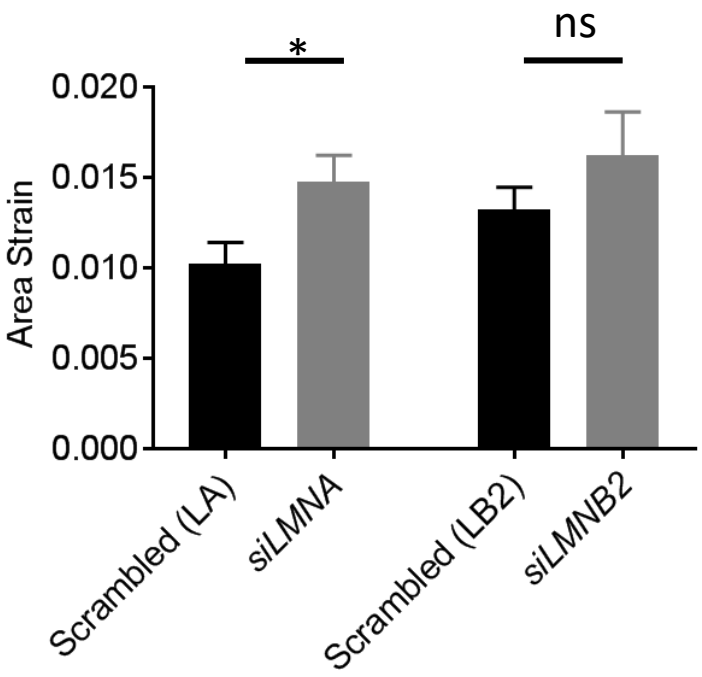
*
ns
0.020
0.015
0.010
0.005
0.000
Area Strain
Scrambled (LA)
siLMNA
Scrambled (LB2)
siLMNB2

Figure S5

A

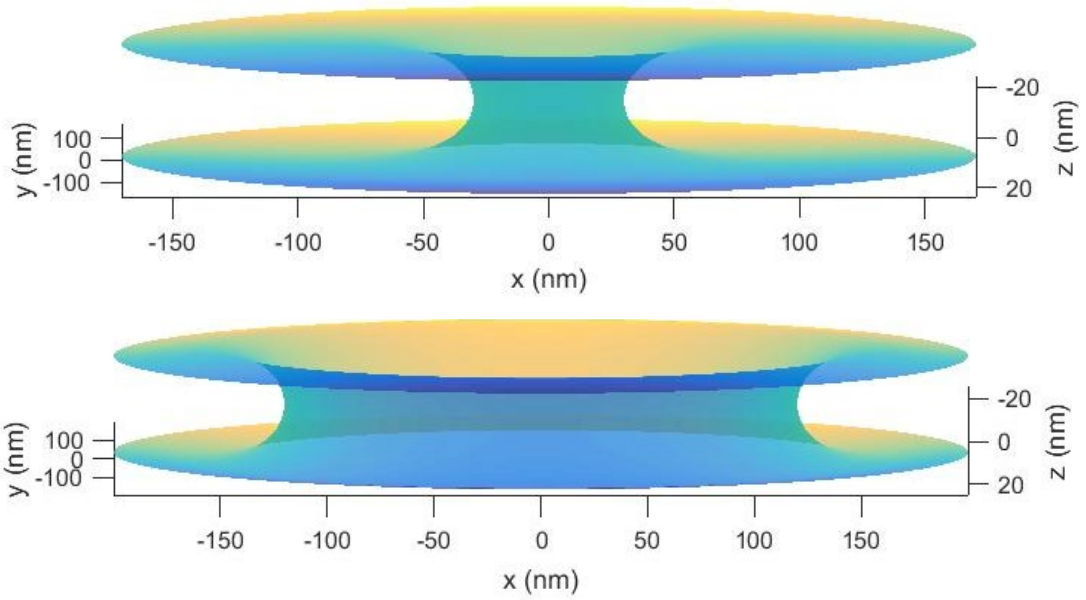
y (nm)
100
0
-100
-150
-100
-50
0
50
100
150
x (nm)
-20
0
20
z (nm)
y (nm)
100
0
-100
-150
-100
-50
0
50
100
150
x (nm)
-20
0
20
z (nm)

B

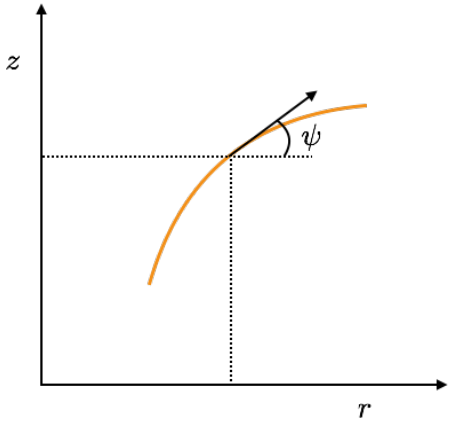
z
ψ
r

Figure S6

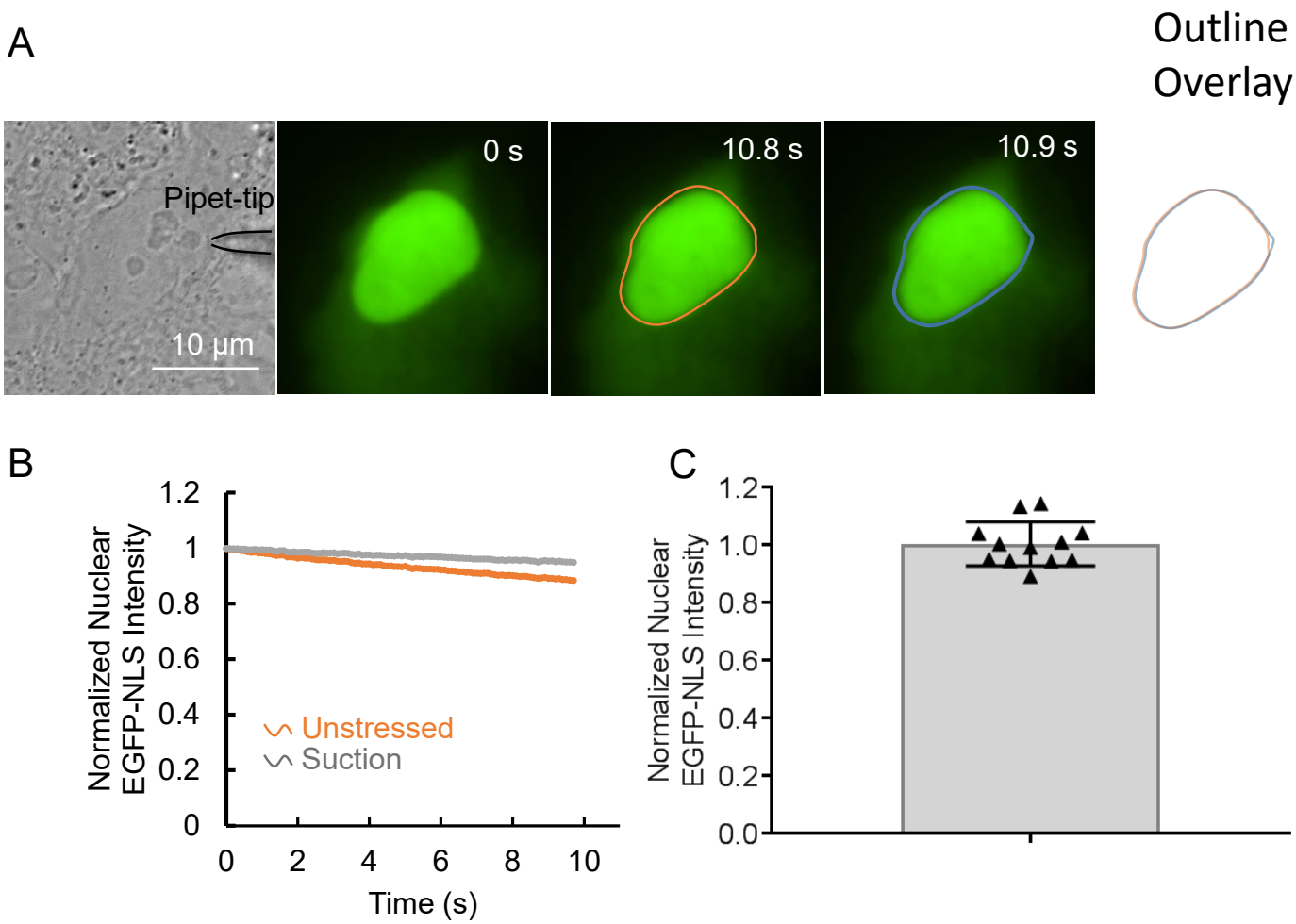
A
Outline
Overlay
Pipet-tip
10 µm
0 s
10.8 s
10.9 s
B
Normalized Nuclear
EGFP-NLS Intensity
1.2
1
0.8
0.6
0.4
0.2
0
Unstressed
Suction
0
2
4
6
8
10
Time (s)
C
Normalized Nuclear
EGFP-NLS Intensity
1.2
1.0
0.8
0.6
0.4
0.2
0.0